Laser Generation of IronDoped Silver Nanotruffles with Magnetic and Plasmonic Properties

Vincenzo Amendola,[1](*) Stefano Scaramuzza,[1] Stefano Agnoli,[1] Gaetano Granozzi,[1] Moreno Meneghetti,[1] Giulio Campo,[2] Valentina Bonanni,[2] Francesco Pineider,[2] Claudio Sangregorio,[2,3] Paolo Ghigna,[4] Stefano Polizzi,[5] Piero Riello,[5] Stefania Fiameni,[6] Luca Nodari[6]

[1]Department of Chemical Sciences, Università di Padova, Padova I-35131, Italy
[2]Department of Chemistry, University of Florence & INSTM, Florence I-50019, Italy
[3]ICCOM-CNR, Sesto Fiorentino, Florence I-50019, Italy
[4]Department of Chemistry, Università di Pavia, Pavia I-27100, Italy
[5]Department of Molecular Sciences and Nanosystems, Università Ca' Foscari Venezia and INSTM UdR Venezia Venezia-Mestre I-30172, Italy
[6] CNR – IENI, Padova I-35127, Italy

Abstract.

A frontier topic in nanotechnology is the realization of multifunctional nanoparticles (NPs), in which multiple properties are simultaneously achieved by the coexistence of different elements of the periodic table. However, the design of nanostructures endowed with multiple functions is inhibited when the required composition is forbidden for thermodynamic reasons. Iron and silver are such an example of thermodynamically immiscible metals whose coexistence at the nanoscale would be highly interesting for the realization of multifunctional NPs, opening the way to a large number of scientific and technological applications ranging from nanophotonics to nanomedicine. Here we describe the synthesis in one-step of Fe-Ag magnetic-plasmonic NPs, by exploiting the fast kinetics of nanomaterials formation peculiar of laser ablation in solution. The NPs are composed by a scaffold of face centred cubic metal silver alternating with disordered Ag - Fe alloy domains and a minority of ultrasmall Fe rich regions, all arranged in a truffle-like nanostructure. Consequently, Fe-Ag NPs show the plasmonic properties of Ag and the magnetic response of iron-containing phases, and the surface of Fe-Ag NPs can be functionalized in one step with thiolated molecules. We took advantage of the multiple properties of Fe-Ag NPs for the 10-fold magnetic amplification of surface enhanced Raman scattering (SERS) signals. The excellent colloidal stability of Fe-Ag NPs allowed also the regeneration and the repeated exploitation of the same particles for multiple SERS analysis. Although with our synthetic approach the control of NPs size and phase is challenging, its great advantages is the general applicability, which virtually permits the preparation in one step of NPs containing all the desired elements, by avoiding the thermodynamic constraints to their miscibility.

Keywords: Plasmonic; Magnetic; Nanoalloy; Silver; Iron; SERS

Introduction.

The frontier of nanotechnology is continuously progressing towards the realization of multifunctional nanoparticles (NPs), in which different properties are achieved by a fine control of nanomaterials structure and composition.[1-3] The addition of distinct elements in the same nanometric "box" is a successful strategy to expand the range of physical-chemical properties available within a single nanotool, and sometimes it allows the discovery of new phenomena and of synergistic performances.[4-6] In particular in the case of plasmonic materials, this concept recently opened the way to the realization of multielement NPs in the form of alloys or heterostructures, where a noble metal with excellent plasmonic response, such as gold and silver, coexists with a metal with magnetic or catalytic properties such as transition metals (Fe, Co, Ni, Ti, Rh) or other "non-plasmonic" noble metals (Pt, Pd).[4-7] In several cases, mutual interactions between the distinct physical-chemical properties of each element are observed, a feature that is highly desirable in fields such as magneto-plasmonics,[8-10] and plasmon enhanced catalysis.[11] The potential application range for these multielement particles is wide, covering for instance the realization of multimodal contrast agents for nanomedicine,[12] selective cargos for drug delivery,[13] theranostic particles,[14] light-triggered antibacterial materials,[15] devices for magneto-optical information processing,[16] new catalysts activated by the sunlight[17] and magnetically recoverable catalysts.[18]

The realization of a nanoalloy is a straightforward approach to achieve multifunctional nanomaterials whenever the desired elements can be mixed in a single phase in ordinary reaction conditions, either for thermodynamic or kinetic reasons.[5,19] When mixing at the nanoscale is not possible, instead, the synthetic strategy proceeds by formation of heterostructures, usually with a multistep process where the crucial role is played by the wettability of the phases containing the two elements.[5,6,20]

Alternatively, one can attempt out-of-equilibrium synthetic approaches to place immiscible elements inside the same nanostructure.[19] Laser ablation synthesis in solution (LASiS) is such an example, since it operates in conditions where the kinetics of NPs formation is very fast and, often, the final phase of the products is not the thermodynamically favoured one.[21,22] In LASiS, a bulk target is immersed in a liquid solution and it is ablated by focused laser pulses.[21] The NPs, which can form either by nucleation and growth of ablated vapours or by solidification of melted drops ejected from the target, are collected as a colloidal solution directly in the liquid.[21] We recently demonstrated the potential of LASiS for the

preparation of magnetic-plasmonic Fe-Au nanoalloys with a composition exceeding the room temperature thermodynamic limit.[23,24] In fact, Fe-Au NPs with same phase and composition had never been obtained before as colloidal solutions by standard synthetic approaches such as the wet chemistry methods.[23] LASiS exploited in particular the fact that kinetically stable bulk Fe-Au alloys can be obtained at room temperature and pressure by melting and fast cooling,[21] thus permitting the transfer of the target phase from the bulk scale to the nanoscale through the fast kinetics of the laser ablation process.

Another attractive example of magnetic-plasmonic material is represented by the Fe-Ag system, since silver has superior plasmonic performances than gold.[5,6,25] Contrary to Fe-Au, however, Fe and Ag do not form thermodynamically stable alloys at any temperature.[26,27] Moreover, kinetically stable Fe-Ag ordered alloys, where iron is present as a substitutional impurity in the face centred cubic (fcc) lattice of silver, or silver replaces iron in its body centred cubic (bcc) lattice, have never been observed in the bulk phase.[26-29] Consequently, the sole examples of bimetallic Fe-Ag nanometric particles consist in the non plasmonic $AgFeO_2$ oxide,[30] or in heterostructures where the plasmonic Ag phase and the magnetic Fe phase (either metal or oxides) are grown during distinct synthetic steps.[6,31,32]

Here we exploited the LASiS to obtain in a single step magnetic-plasmonic Fe-Ag NPs. Composition, structure and shape of NPs retain the traces of the fast kinetics of particles' formation, and this allowed the inclusion of magnetic and plasmonic phases within the same nanometric object. The multifunctionality of Fe-Ag NPs opens the way to a series of applications and, for instance, we demonstrate that magnetic amplification of the surface enhanced Raman scattering (SERS) is possible with our systems. The surface of Fe-Ag NPs can be functionalized in one step with thiolated molecules, by formation of sulphur-silver chemical bonds, thus enabling another degree of freedom to improve their properties. For instance, surface functionalization was used to impart colloidal stability to Fe-Ag NPs, which was crucial for the realization of a magnetically responsive SERS system which can be regenerated and used for repeated Raman analysis with different analytes.

In general, our results demonstrate that LASiS can be a general approach for the preparation in one step of multielement NPs, bypassing the thermodynamic limitations to miscibility and, thus, providing an innovative and versatile method to access a wide range of new multifunctional nanostructures.

Results.

Synthesis and characterization.

Fe-Ag NPs were obtained by LASiS with near infrared (1064 nm) pulses (Figure 1a), starting from a

bulk bimetallic target with composition 34at% of metal Fe (average grain size of 34 nm) and 66at% of metal Ag (average grain size of 71 nm). The laser ablation was performed in two distinct liquids (water or ethanol), which are environmentally friendly, thus contributing to make the overall synthetic procedure compatible with the principles of "green" chemistry.[33] Besides, we selected water and ethanol because both of them were previously used for the LASiS of silver[21,34] or iron-containing[21,35] NPs.

Laser generated Fe-Ag NPs were mixed with a solution of PEG and EDTA, kept at 30°C for 1 hour, dialysed and finally resuspended in distilled water. Thiolated PEG can chemically bind the surface of Fe-Ag NPs, by the formation of sulphur-silver chemical bonds,[36] providing stability to the colloidal system in several polar and non polar liquids. EDTA is required to remove synthesis by-products like amorphous/crystalline iron oxides and hydroxides, as usually done with iron-based NPs obtained by LASiS.[23,37] In this way, only the PEG-coated NPs remains in solution after the dialysis step by centrifugation in 10 kDa concentration membranes. The effective coating with PEG, assessed by Fourier transformed infra-red (FTIR) spectroscopy, is immediately appreciable by the yellow-green colour of the Fe-Ag NPs solution collected after dialysis, which actually is typical of colloidal silver[25,36] (Figure 1b). In fact, the optical absorption spectrum of the Fe-Ag NPs solution show a sharp peak at about 410 nm, due to the surface plasmon resonance (SPR) of silver[25,36] (Figure 1c-d). The optical properties of Fe-Ag NPs do not change even several weeks after their preparation, thus assessing the stability in time and in aqueous solution of our nanomaterials.

The magnetic responsivity of Fe-Ag NPs is evident by their accumulation in proximity of a small NdFeB magnet placed close to the cell containing the nanoparticle dispersion (Figure 1b). Together with the colloidal stability of Fe-Ag NPs, this allowed the magnetic sorting in two fractions, one with stronger magnetic response (magnetic, M), and another one which did not respond to the magnetic field in the time interval of the experiment (non magnetic, NM). Importantly, the SPR is present also in the M phase (Figure 1c-d), clearly indicating that the plasmonic silver phase coexists with the magnetic iron phase. Compared to the "non magnetic" fraction, the SPR of "magnetic" Fe-Ag NPs is broader and red shifted of ~25 nm, which is compatible with the presence of particles with size larger than ~50 nm or with non-spherical shape,[25] whereas the sharp plasmon band at 400nm observed in the NM fraction is typical of spherical Ag NPs with size below ~50 nm.

The comparison of the optical absorption spectra gives information about the partition of the plasmonic silver phase between the M and NM fractions (Figure 1c-d). According to the absorbance at the SPR maximum, about 30% of the SPR signal is present in the M fraction of NPs synthesized in ethanol,

while only 20% is found in the M fraction of NPs obtained in water. This suggests that ethanol is better than water for the realization of magnetic-plasmonic NPs, in agreement with previous studies about the LASiS of Fe-Au NPs, where optimal alloying was observed in pure ethanol, whereas metal Au particles with only a few percent of Fe were obtained in water.[24] Therefore, the structural investigation was focused on the best sample, consisting of Fe-Ag NPs obtained in ethanol.

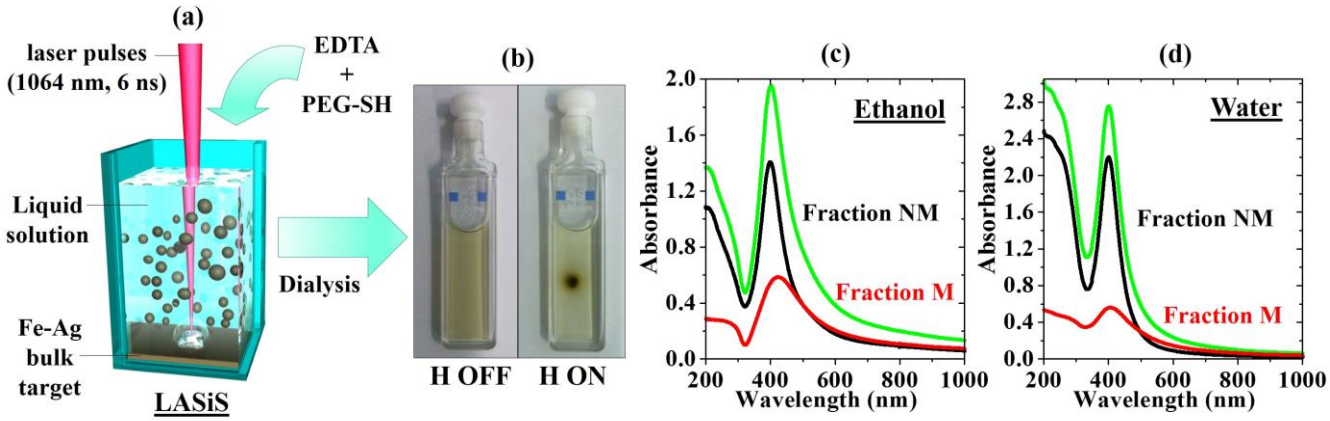

Figure 1. Sketch of LASiS (a) and pictures (b) of Fe-Ag NPs solution showing the yellow-green colour typical of plasmonic silver and the accumulation of NPs by the magnetic field H, applied by placing a small NdFeB magnet on one side of the cuvette. (c-d) OAS spectra of PEG-coated Fe-Ag NPs synthesized in ethanol (c) or water (d) and redispersed in water just after the synthesis (green line), and after the magnetic sorting in fractions M (magnetic, red line) and NM (non-magnetic, black line).

In order to obtain structural information at the level of the single NP, Fe-Ag NPs were investigated by transmission electron microscopy (TEM). Fraction M is composed by relatively large NPs (Figure 2a), with average size of 103±44nm, while NPs in fraction NM are smaller (Figure 2b). The size distribution of fraction NM is bimodal, with an intense peak for small NPs centred at ~5nm and a broad population of large NPs ranging from 10 to 50 nm. In addition, a remarkable morphological difference exists between NPs in the two fractions: in fraction M, NPs have a truffle-like structure since they appear as the agglomeration of smaller clusters partially fused together, originating particles with irregular surfaces (Figure 2a,c), whereas NPs in fraction NM are mostly spherical or rounded (Figure 2b). The difference of shape agrees very well with the different optical properties of M and NM fractions, reported in Figure 1c, since a broad and red shifted SPR is compatible with truffle-like silver NPs, whereas a sharp SPR at 400 nm is compatible with spherical NPs.[25] This was further assessed by numerical calculations of the optical properties of silver NPs with spherical or truffle-like structure, reported in Figure 2d, where SPR broadening and red shift is clearly observed at parity of size and dielectric environment, just by changing the shape from a perfect sphere to a nanotruffle.

The selected area electron diffraction (SAED) pattern taken on a single representative Fe-Ag NPs (see Figure S1 in S.I.) is dominated in intensity by the reflections of fcc silver, but it is also rich of several other low intensity reflections whose precise identification is difficult and which are compatible, for instance, with metal and oxide iron phases as well as with various Fe-Ag alloys. Importantly, in all Fe-Ag NPs of fraction M, both Ag Lα (3.0 keV) and Fe Kα (6.4 keV) peaks are found by energy dispersive X-ray spectroscopy (EDS, Figure 2e). This was further substantiated by line scan EDS mapping on a cluster of NPs (Figure 2f), showing that Fe Kα and Ag Lα signals are overlapped. In particles of fraction NM, instead, the Ag signal was the only one detected, with a few exceptions (~5%) corresponding to >50nm NPs, where weak iron peaks were found together with a largely dominating silver signal. This clearly explains the different magnetic response of NPs in the M and NM fractions: since the attractive magnetic force scales with the mass of the magnetic material,[38] those NPs with negligible content of iron or with small size were not attracted by the magnetic field, contrary to those NPs where an appreciable amount of iron coexists with silver.

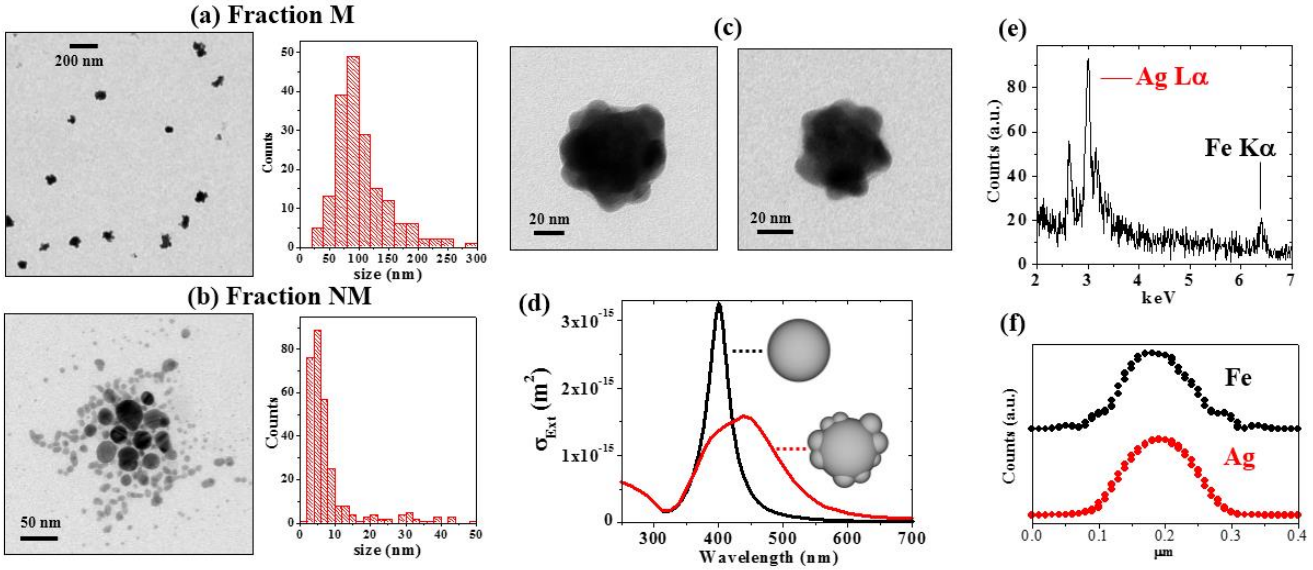

Figure 2. TEM images and size histograms of Fe-Ag NPs in fraction M (a) and NM (b). Two representative Fe-Ag NPs of fraction M are reported in (c), showing the typical truffle-like structure resembling a partially melted aggregate of smaller clusters. (d) Numerical simulation of the extinction cross section of a spherical 25nm Ag NP and of an Ag nanotruffle with the same volume, both in water matrix. (e-f) Representative EDS spectrum (e) and line scan intensity (f) of the Ag L lines and Fe K lines collected on Fe-Ag NPs from fraction M.

The iron content in the Fe-Ag NPs of fraction M was quantitatively assessed by inductively coupled plasma assisted mass spectrometry (ICP-MS) and resulted of 15at%, which is lower than the bulk target

content (Fe 34at%). This means that part of Fe was removed during the purification/dialysis step, in agreement with our previous observation about the LASiS of Fe-Au NPs.[23,24]

The chemical composition of Fe-Ag NPs (fraction M) was further investigated by x-ray photoelectron spectroscopy (XPS), revealing the presence of sulphur, carbon, silver, oxygen and iron photoemission lines. Sulphur *2p* (Figure 3a) and carbon *1s* (Figure 3b) peaks are due to the shell of thiolated ligands surrounding the NPs, further confirming the coating of Fe-Ag NPs with the stabilizing layer. In case of the carbon *1s* spectrum, there is no signal at the binding energy (BE) of carbides (283.0-283.6 eV),[39] suggesting that iron carbide is not present (Figure 3b). The photoemission line of Ag ($3d_{5/2}$ peak) has a main chemical component centred at a BE of 368.4 eV, which is the typical Ag(0) value expected for plasmonic silver.[40] The Fe 2*p* photoemission spectrum, reported in Figure 3d, is constituted by several different components with a complex multiplet structure. Although the identification of a prevailing component is not possible, the Fe $2p_{3/2}$ peak is located at the BE typical of oxides and hydroxides (709-714 eV), with a tail at values often observed in alloys between metal iron and other noble metals (708 eV).[24,41-43] In order to probe the chemical nature inside the Fe-Ag NPs, the sample was sputtered for 10' with Ar^+ (1 keV), after that we observed the increase of the silver and iron component and a concomitant strong decrease of the carbon signal, due to the erosion of the ligand shell. Importantly, a shoulder appears at 707-708 eV in the iron signal (red line in Figure 3d), which is the value typical of metal iron.[44] Therefore, iron at the surface of the Fe-Ag NPs is almost completely oxidised, whereas a mixture of metal and oxidised iron is found inside the particles. The surface layer of oxide is useful for the passivation of Fe-Ag NPs, as recently found also for Fe-Au nanoalloys obtained by LASiS,[24] and it explains the time stability of optical and colloidal properties observed for several weeks after synthesis.

The presence of a complex multiplet structure in the photoemission spectrum of Fe suggests that iron phases are disordered and there is not a dominating crystalline phase. Hence, we performed the w-ray diffraction (XRD) analysis on the "magnetic" Fe-Ag NPs to obtain more information about sample's crystallinity. The XRD pattern (Figure 3e) clearly shows all the peaks of fcc silver, but no reflections ascribable to iron phases are found. This marks a remarkable difference with the XRD pattern of the original target, where the reflections of both metal Ag (fcc) and Fe (bcc) are present (see Figure S2 in S.I.).

The content of Fe in the Fe-Ag NPs measured by ICP-MS and EDS is about 15 times the XRD detection limit of crystalline iron phases with size larger than ~5-3 nm in our experimental conditions. In agreement with XRD, also Raman and FTIR spectroscopic analysis on Fe-Ag NPs excluded the presence of iron oxides with large (e.g. >5-10nm) crystalline grains. Therefore, our results recall

previous studies in thin Fe-Ag films[45,46] where the iron-containing phase is amorphous or is organized in ordered domains with extremely small size, i.e. with high defectivity due to the large surface-to-volume ratio.

Even in the case of heterogeneous or amorphous samples, Mössbauer spectroscopy provides valuable information about the chemical environment and the crystalline order around Fe atoms.[26] The spectrum of the Fe-Ag NPs, reported in Figure 3f, reflects the structural complexity suggested by the previous characterization techniques, being dominated by an intense absorption close to 0 mm/s and by a broad magnetically splitted component. The best fitting was obtained by means of four components (see Figure 3f and Table S1 in S.I.): one doublet and one singlet for the central absorption and two broad sextets for the magnetically coupled component. The doublet (δ close to 0 and Δ to 0.30 mms^{-1}) is typically observed in superparamagnetic systems due to the lack of stable magnetic moment with respect to the ultrafast interaction time of the Mössbauer measurement, and it is compatible with disordered solid solutions of metal Fe and Ag.[28,29,47,48] In Fe-Ag thin films, this doublet is attributed to disordered crystalline sites prevalently located at the grain boundaries between fcc Ag crystals.[29,49,50] The presence of a singlet, with a quite high δ, can be ascribed to Fe atoms incorporated in to Ag-rich regions. The high value of δ (0.68 mms^{-1}) reflects the increase in electron density at the nucleus, due to the presence Ag rich surroundings.[47] Concerning the magnetically splitted components, both are compatible with iron atoms in iron-rich crystalline regions with two slightly different Fe concentrations.[49,50] Therefore, the spectrum describes 3 different types of environment for the Fe atoms in Fe-Ag NPs: *i)* a minority of Fe atoms in a metal iron bcc lattice with nanometric grain size, *ii)* a majority of Fe atoms in disordered sites, which are compatible with the mixed environment of Fe and Ag atoms typical of a bimetallic alloy of the two elements, and *iii)* an intermediate quantity of Fe atoms in an environment composed prevalently of Ag atoms, which is compatible with a diluted alloy of Fe in the metal Ag lattice.

In agreement with all the previous characterization techniques, the Mössbauer spectrum does not indicate the presence of ordered iron oxide crystalline domains with concentration large enough to be detected. This means that surface iron oxide is prevalently amorphous and represents a minor fraction of the total iron present in the sample, likely contributing to the background of the Mössbauer spectrum.

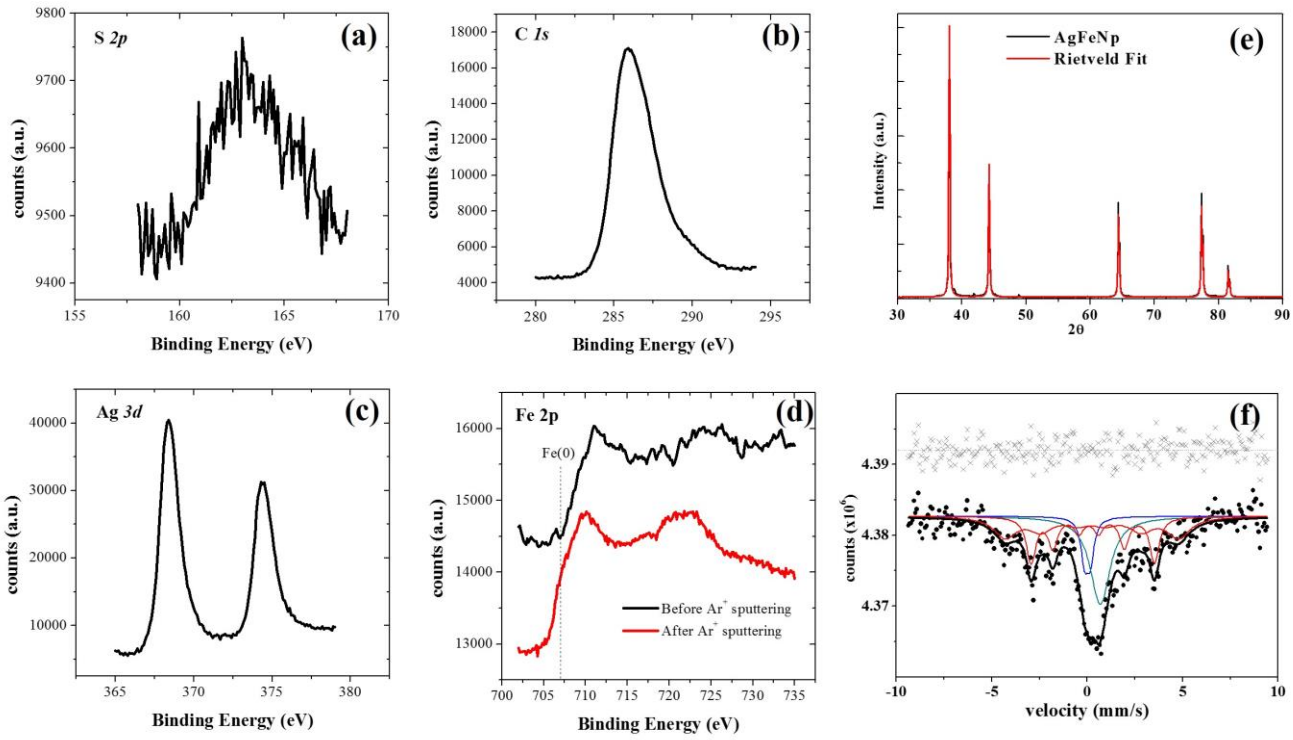

Figure 3. (a-d) X-ray photoemission S 2p (a), C 1s (b), Ag 3d (c) and Fe 2p (d) peaks. (e) XRD pattern of the Fe-Ag NPs of fraction M (black line) and relative Rietveld fit (red line). (f) Mössbauer spectrum of the Fe-Ag NPs fitted with four components (for details see text). Grey crosses are fit residuals.

The discrimination of crystalline environment in the Fe-Ag alloy (i.e. bcc-like or fcc-like) is not possible by room temperature Mössbauer spectroscopy, therefore the intermetallic nature of the Fe-Ag NPs was further substantiated by Synchrotron X-ray Absorption Spectroscopy (XAS). Figure 4 shows the XANES (x-ray absorption near edge structure, a), the EXAFS (extended x-ray absorption fine structure, b) spectra and the corresponding EXAFS Fourier Transforms of the Fe-Ag NPs (c). For what concerns the XANES (Figure 4a), the energy position and shape are strongly dependent on the electron count and structure on the photoabsorber and, in particular, the edge shifts at higher energy with increasing of its oxidation state. Comparison with the XANES of a metallic Fe foil and of Fe_2O_3 shows

the presence of Fe in the Fe(0) oxidation state. In addition, in the pre-edge region, where the 1*s*→3*d* transitions are located, the clear appearance of a Fermi level demonstrates that Fe is present in the metallic state. However, a closer inspection of the XAS spectrum of this sample, shows remarkable differences with respect to that of bulk metallic Fe. In particular, the EXAFS and XANES oscillations after the edge are much dumped when compared to bulk metallic Fe. This is a clear indication that the local atomic environment of Fe is disordered, due to a different chemical environment. As a matter of fact, the EXAFS spectrum (Figure 4d) can be fitted by a structural model in which a minor part of Fe is in the bcc structure of α-Fe, and the rest (the majority of Fe atoms) is surrounded by Ag atoms in an arrangement deriving from the fcc structure of Ag. The fit according to this structural model is shown in Figure 4d and the results are summarised in Table S2 in S.I.. The quite large values for the EXAFS Debye-Waller factors for all the coordination shells confirms the overall disordered structure around Fe atoms in the NPs. Nonetheless, we found an EXAFS goodness of fit (GOF) of 29 %, which, considering the unavoidable noise level in the spectrum, points to a fair agreement between experiment and structural model.

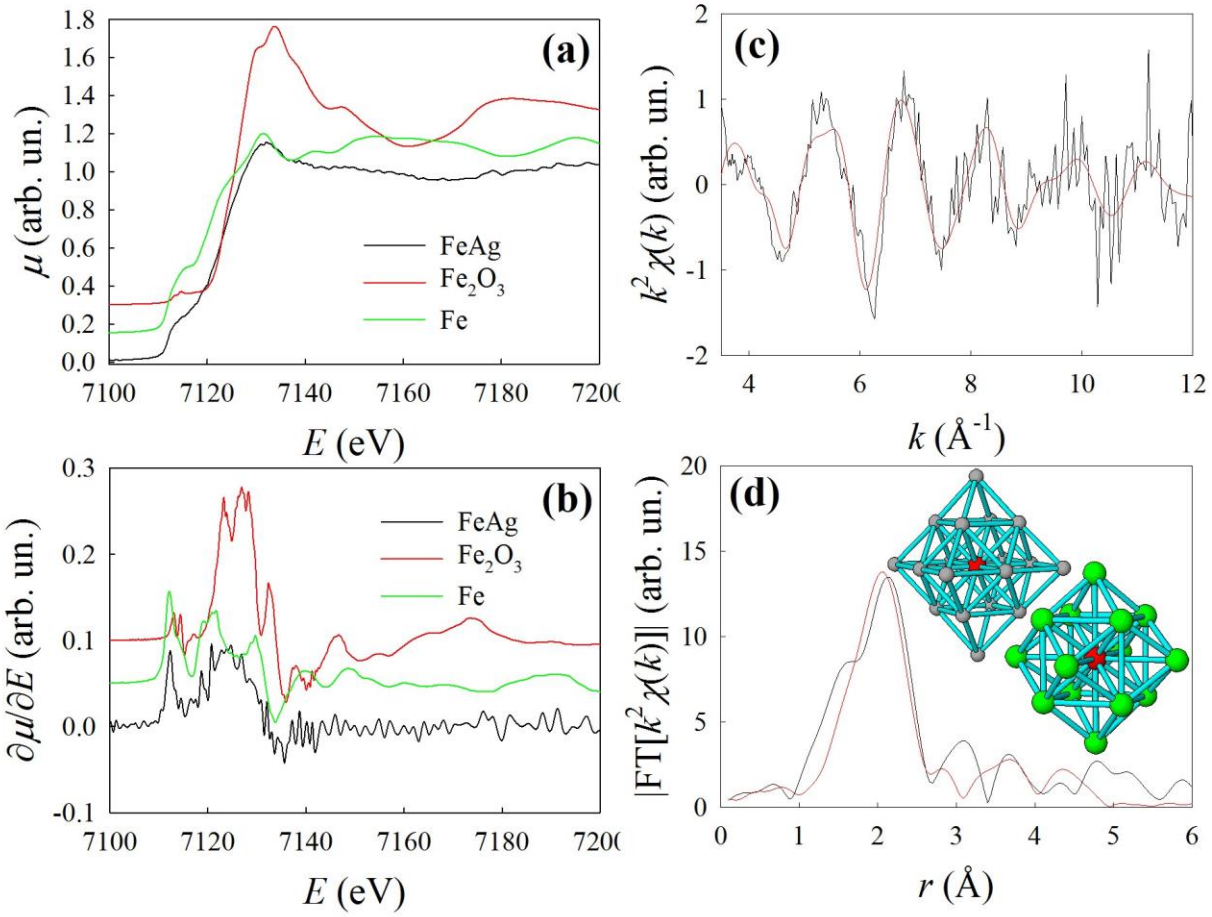

Figure 4. a) XANES Fe-K edge spectrum of the sample investigated in this work. The spectra of bulk

metallic Fe and of an Fe oxide (Fe_2O_3) are also shown for better reference; for the sake of clarity the spectra have been shifted along the *y* axis. b) EXAFS derivative spectra. c) Fourier transformed EXAFS spectrum of the sample investigated in this work (black line), and its fit (red line) according to the model of Table S2 in S.I.. d) EXAFS Fourier transformed modulus and the two clusters used in the fits: red: photoabsorber; green: bcc Fe; gray: fcc Ag.

Since the Fe-Ag NPs are responsive to the application of an external magnetic field and structural analysis evidenced the presence of metallic Fe and disordered Ag-Fe phases, the sample of fraction M was investigated quantitatively by SQUID magnetometry at 300 K and 2.5 K. The hysteresis loop collected at room temperature (Figure 4) is fully reversible and the magnetization, at the highest measuring field is 0.9 Am^2/kg. Conversely, at low temperature (2.5 K) the loop is open with a coercive field of ~30 mT, a reduced remanent magnetization of 0.11 and a high field magnetization of ca. 1.5 Am^2/kg at 5 T The observed magnetic behaviour is consistent with the presence of nanometric single domain magnetic particles which are blocked at low temperature and enter the superparamagnetic state at room temperature. However, the low value of the measured magnetic moment and the small remanence at low temperature suggest that most of NPs are made of disordered Fe-Ag alloy.[51]

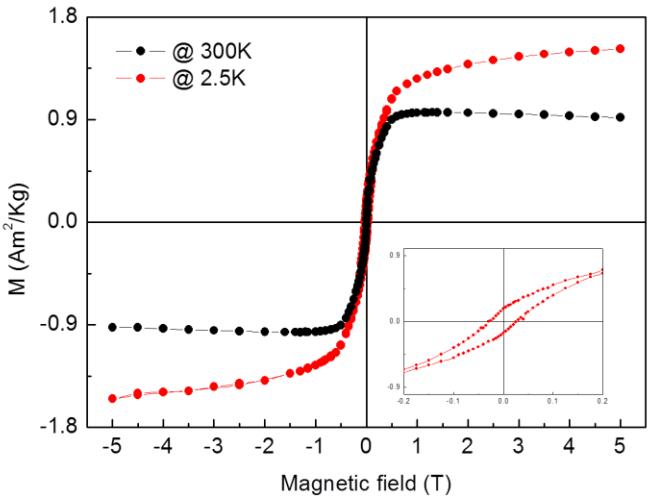

Figure 5. Hysteresis loops collected at 300 K and 2.5 K of Fe-Ag NPs in fraction M. The inset is the enlarged loop measured at 2.5K.

Magnetic amplification of SERS signals.

Since we obtained a multifunctional nanomaterial endowed with magnetic and plasmonic properties and a complete colloidal stability, we used all these features in a synergistic way for a practical application: the detection of organic molecules by SERS.

Magnetic amplification of SERS with Fe-Ag NPs was investigated at 633 nm with a micro-Raman spectrometer, by adding a cationic dye (malachite green, MG) to the particles dispersion. In a typical experiment, SERS measurements were performed before (H=0) and after (H>0) the application of a small NdFeB magnet in the point of analysis. In this way, the Fe-Ag NPs were reversibly focused by the external magnetic field on an area as small as the face of the magnet.

The intensity of the magnetophoretic force scales with the size of the object,[38] hence the use of a selective sedimentation protocol is crucial for the selection of Fe-Ag NPs with large mass and maximum responsivity to the magnetic field. It is worth pointing out that also SERS performances are size-dependent, with an optimum in the 50-70 nm size range.[52,53] Hence, for optimal results, we used the fraction collected by selective sedimentation after centrifugation at 126 rcf, which meets the above requirements because it contains NPs with average size of 73±23 nm.

MG is a cationic molecule which can interact with negatively charged NPs and, indeed, by Z-spectroscopy, we found that the Fe-Ag NPs have a negative Z-potential of -26±5 mV. Being Fe-Ag NPs coated with PEG, the addition of the cationic analyte does not induce the coagulation of the colloid, which instead remains stable.

As shown in Figure 6a, the Raman spectrum collected on the quartz cuvette containing the Fe-Ag NPs mixed with MG is 10 times more intense after magnetic focusing, allowing the detection of a bright signal even at analyte concentration as low as $8 \cdot 10^{-8}$ M (ca. 40 picomols of analyte).

Contrary to solvent drying on a solid substrate, which is commonly used for the concentration of SERS active nanomaterials, magnetic focusing can be performed within the colloidal dispersion in an optical cuvette. In this way, the process can be repeated multiple times, and the SERS substrate can be regenerated, namely the analyte can be removed and the substrate reused virtually for an unlimited number of times. This is demonstrated in Figure 6b, where we show the magnetically amplified SERS spectra collected on Fe-Ag NPs by cyclically alternating two different cationic analytes (MG and HITC, both at the same molar concentration of $8 \cdot 10^{-8}$ M). Before changing analyte, Fe-Ag NPs were subjected to a simple regeneration procedure consisting in centrifuge washing with water. Raman measurements on regenerated Fe-Ag NPs prior to the addition of the next analyte show no signal, while an intense spectrum is found each time after the addition of the analyte and magnetic focusing of NPs. The magnetic amplification of SERS signal is reproducible throughout all the measurements of Figure 6b, and it was of 10±3 for MG and 14±6 for HITC.

Interestingly, we found that PEG coating plays a relevant role on the SERS amplification induced by the magnetic-field. As shown in Figure 6c, a 2-fold increase of the magnetic amplification is obtained

by adding PEG at concentration lower than 0.003 mg/mL during the synthesis, while the amplification reaches a plateau for a PEG concentration larger than 0.01 mg/mL, suggesting that this is the threshold required for a complete coating of Fe-Ag NPs surface. We also probed the effect of PEG molecular mass, namely of its chain length, on the magnetic amplification process, by keeping unchanged the PEG molar concentration to 2 μM (equivalent to 0.01 mg/mL for 5000 Da PEG) and using either a 2000 Da or a 20000 Da PEG. As shown in Figure 6d, shortening the PEG chain to 2000 Da has a positive effect, corresponding to the doubling of the magnetic amplification of SERS signal (23±10 for 2000 Da versus 9±1 for 5000 Da), while the effect is negative by using the 20000 Da PEG, because the magnetic amplification is reduced to 6±2.

Magnetic focusing of Fe-Ag NPs can amplify the Raman signal both by increasing the local concentration of the SERS substrates loaded with analyte and by formation of new electromagnetic hot spots when the plasmonic nanostructures are collapsed together due to the attractive magnetic force. Although PEG chains are indispensable for the stability of Fe-Ag NPs and the reversibility of the magnetic amplification, they also have the effect of increasing the hydrodynamic friction coefficient of the nanostructure, thus opposing to particle migration under the action of the magnetic force. Besides, PEG mechanically hampers the coalescence of Fe-Ag NPs when they accumulate in proximity of the magnet, thus limiting the formation of electromagnetic hot spots. Finally, the density of PEG coating may interfere with the absorption of cationic molecules on the Fe-Ag NPs, because a limited portion of NPs surface is available for analyte adsorption when the surface density of PEG reaches its maximum. Taken together, the above considerations can explain the observed increase of magnetic amplification for decreasing PEG coating and chain length. To gain more insight about the prevailing amplification factor, we measured the efficiency of magnetic migration, expressed as the ratio of absorbance at the surface plasmon resonance maximum (~425 nm) before (Abs(B=0)) and after (Abs(B>0)) magnetic focusing of Fe-Ag NPs on the bottom of the cuvette, as a function of PEG chain length. The Abs(B=0)/Abs(B>0) was of 0.20, 0.30 and 0.27 for, respectively, 2000 Da, 5000 Da and 20000 Da PEGs. Since the migration efficiency does not depend on PEG length, it is likely that long polymeric chains oppose to the formation of hot spots or to the adsorption of cationic molecules on NPs surface, with consequent decrease of the SERS performances.

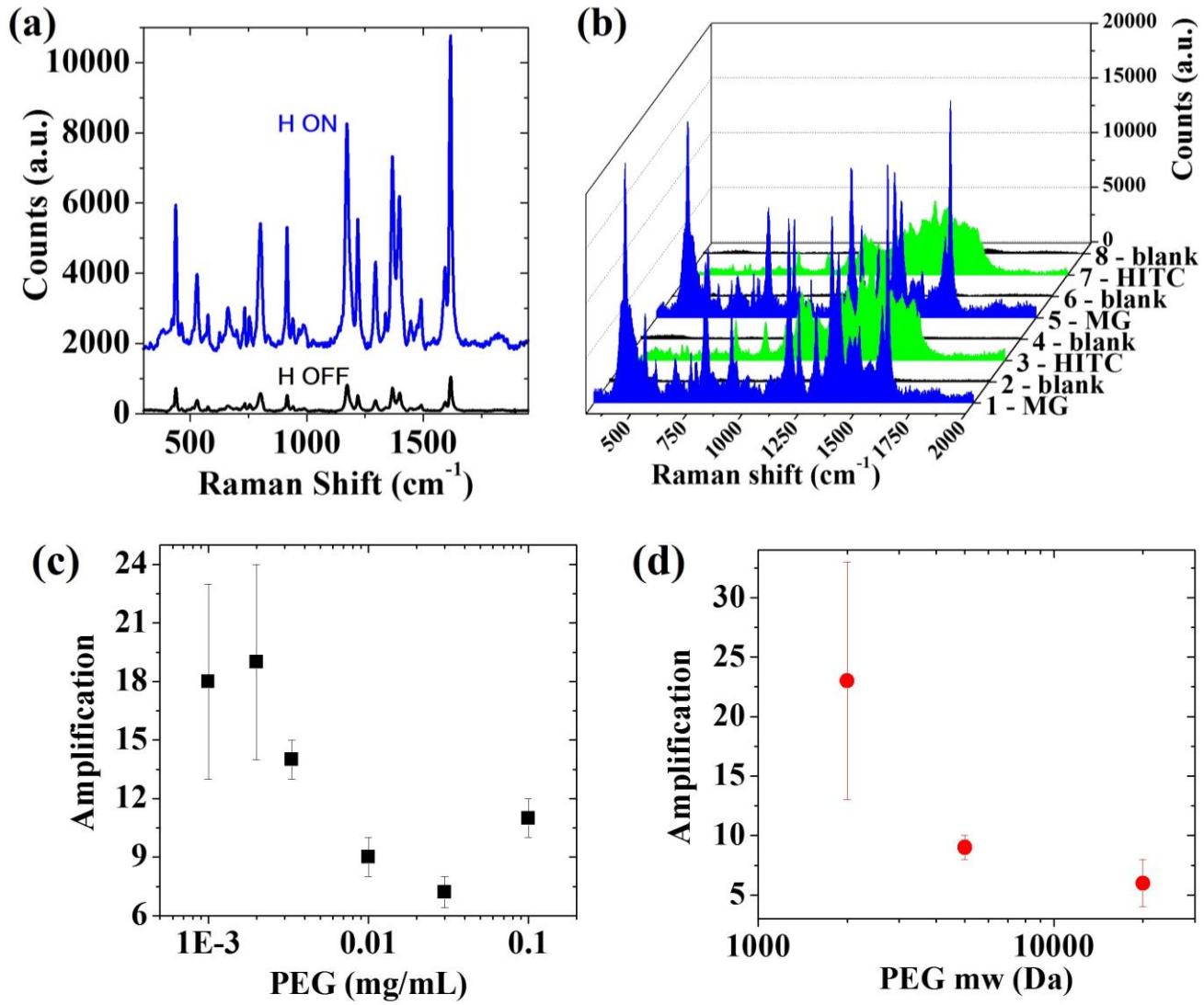

Figure 6. (a) Raman spectra of the MG/Fe-Ag NPs dispersion before (H=0, black line) and after (H>0, blue line) magnetic focusing. Spectra are vertically shifted for clarity. (b) Raman spectra of magnetically focused (H>0) Fe-Ag NPs dispersion: mixed with MG (1, blue line), after regeneration procedure (2, black line), mixed with HITC (3, green line), after second regeneration procedure (4, black line), mixed with MG (5, blue line), after third regeneration procedure (6, black line), mixed with HITC (7, green line) and after the fourth regeneration procedure (8, black line), ready for the next analyte. c) Magnetic amplification of SERS signal as a function of PEG concentration during the Fe-Ag NPs coating procedure. d) Magnetic amplification of the SERS signal as a function of PEG molecular weight (at parity of PEG concentration).

Discussion

Formation mechanism of Fe-Ag NPs.

Our structural investigations confirmed that NPs of fraction “M” are actually composed of silver and iron. In particular, XRD and SAED identified crystalline fcc silver as the dominating ordered phase, whereas TEM, Mössbauer and EXAFS revealed that iron is mostly present in disordered Fe-Ag alloy

domains, which are not detectable by XRD. However, iron atoms located at the surface of NPs inevitably undergo oxidation, as assessed by XPS. The Fe-Ag NPs basically are superparamagnetic at room temperature, and we exploited the coexistence of magnetic and plasmonic properties for the amplification of SERS performances

According to Fe-Ag phase diagram, the two metals are immiscible both in the solid and in the liquid phase.[26] Contrary to other cases of bimetallic compounds, which can be obtained as kinetically stable ordered alloys despite the unfavourable thermodynamics,[12,22,23] the Fe-Ag system only form disordered alloys, even when out-of-equilibrium synthetic approaches such as sputtering are used.[26-28,46] At the nanoscale, silver nanocrystals with size larger than ~5 nm have the same structural constraints of bulk or thin film equivalents,[54,55] therefore the same miscibility limitations of the bulk Fe-Ag system is valid for Fe-Ag NPs.

In addition, the morphology and the chemical composition of our Fe-Ag NPs retain the traces of the fast kinetics of formation occurring with LASiS. In LASiS, the laser pulses focused on the bulk target extract the matter by generation of a plasma plume, on a time scale of few ps, which expands in the liquid buffer over a time of hundreds of ns, releasing heat to the surrounding solution and forming a cavitation bubble that expands and collapses on a timescale of hundreds of microseconds.[21] The exact mechanism of NPs formation is still object of intense theoretical and experimental investigations,[21,56] and it is highly dependent on the system parameters such as the laser pulse duration and energy.[21] However, there is a large number of evidences that nanomaterials obtained by LASiS form by the coalescence of smaller crystalline nuclei with nanometric size.[21] These nuclei can be extracted directly from the target, or can form by nucleation of atomic and molecular vapours present in the plasma plume.[21] In the case of a target composed of a single element (such as pure Ag)[36] or miscible elements (such as Ag and Au),[57,58] the coalescence of pristine nuclei generates spherical or rounded NPs, due to the high temperature in the LASiS environment and the consequent high mobility of atomic species on the surface of NPs. In fact, the formation of spherical shapes is the way the interface energy is minimized during the synthesis of metal NPs.[59,60] In the present case, however, the lack of miscibility between Ag and Fe is the reason for the formation of new interfaces between distinct phases inside the same NP, whose energetic cost is comparable to the formation of solid-liquid boundaries. This is reflected in the formation of clustered NPs with truffle-like shape, where it is still possible the identification of pristine nuclei forming the final NP. In addition, the diffusivity inside NPs is hampered by the presence of multiple dislocations and boundaries between grains with different crystalline structure, such as fcc silver, bcc iron and amorphous Ag-Fe alloy. The final result is the

formation of NPs with an intermediate shape between the sphere and the fractal cluster obtained by diffusion limited aggregation of laser-generated nanometric nuclei. From this point of view, the synthesis of Fe-Ag NPs represents an excellent opportunity to freeze and study the coalescence step of LASiS. In particular, the truffle-like morphology of Fe-Ag NPs suggests that nuclei temperature is close to the melting point when their coalescence takes place, and that the process is fast enough to run out of thermodynamic equilibrium, where pure Ag, Fe and iron-oxide phases are favoured.

The chemical composition of Fe-Ag NPs, evidenced for instance by XPS analysis, is the result of the highly reactive environment present in the plasma plume, containing species from the target and species from the solution, all at high temperature, high pressure and in ionized condition.[21] For instance, the formation of Fe_xAg_y bimetallic clusters has been observed during the pulsed laser irradiation of mixed Fe and Ag powders in gas phase,[61] despite the lack of miscibility of the two metals. This suggests that the same species can be formed in liquid solution. In the present case, however, the solution contains solvent molecules and the dissolved atmospheric gas such as O_2, CO_2, N_2 and H_2O,[21,35] and the plasma plume acts as an oxidising environment each time that the concentration of oxidising species in solution is high. For instance, noble metals NPs such as Au, Ag and Pt NPs obtained by LASiS in aqueous solutions undergo partial surface oxidation,[21] and laser ablation of pure metal iron in water yields iron oxide NPs.[37,62] Therefore, in the case of the Fe-Ag system, the ablated metal iron atoms can readily react with oxygen in the plasma plume, forming different types of oxides with stoichiometry depending on the local concentration of oxidising species. In any case, at times longer compared to the laser ablation dynamics, metal iron on the surface of Fe-Ag NPs will react with oxygen, whereas iron atoms inside the NPs are protected by the external layer of metallic silver and iron oxide. Importantly, oxidation of iron in coalescing nuclei is also compatible with the observation of Fe-Ag NPs with irregular shapes, because iron oxide creates metal-oxide interfaces and hampers the diffusion of metal atoms necessary to the formation of rounded nanostructures.

The synthesis of Fe-Ag in an oxidising solvent such as water gives a lower yield of Fe-Ag NPs, i.e. a higher yield of separated Ag and Fe NPs, than in ethanol. This suggests that, in the stage of nuclei coalescence, the sticking coefficient upon collision of silver nuclei with iron oxide nuclei is lower than between the nuclei of metal silver and metal iron. A similar effect may take place during the nucleation stage, if distinct nuclei of silver and iron oxide form instead of bimetallic silver-iron nuclei. Overall, there is a clear indication that iron oxidation should be avoided during LASiS to achieve the coexistence of the two immiscible elements in the same NP.

Even with LASiS in ethanol, the yield of Fe-Ag NPs does not reach the 100%, and this can be explained with the asymmetry of the reaction conditions intrinsic in LASiS. LASiS is characterized by the formation of four gradients (temperature, pressure, target species concentration and solution species concentration) steeply varying in time and space.[21] In particular, the concentration of solution species increases by getting far from the ablation site, whereas the concentration of target species increases by approaching the ablation site. The same trend occurs for increasing time after the ablation event. Therefore, the probability of reaction between iron and oxidising solution species is higher at the borders of the plasma plume and for longer times after the ablation event: these are the conditions where the formation of distinct silver and iron NPs are more probable during laser ablation of the Fe-Ag target in ethanol. Hence, it is likely that the yield of Fe-Ag NPs can be further improved by avoiding the presence of oxidising species, such as atmospheric oxygen and water molecules, during the synthesis.

In summary, the experimental results agree with the formation of Fe-Ag NPs by the following mechanism (Figure 7):

i) Formation of nuclei (Figure 7a). After laser ablation of the target, hot nuclei containing Ag, Fe and mixed Ag and Fe are formed. In water, oxidation of iron occurs with high probability, whereas in ethanol this process is less probable due to the lower concentration of oxidising species.

ii) Nuclei coalescence (Figure 7b). Hot nuclei coalesce together and quickly cool down, forming solid NP. However, due to the high concentration of defects and dislocations, NPs have the structure of a "melted fractal" aggregate, i.e. of a nanotruffle. At borders of the plasma plume, due to the higher concentration of oxidising species from the solution and lower concentration of target species, there is higher probability that iron is oxidised and a consequent lower probability of sticking with silver nuclei, thus avoiding the coexistence of iron and silver in the same nanostructures.

iii) Surface oxidation of NPs takes place by interaction with the hot solution species, prosecuting also at room temperature by interaction with atmospheric oxygen or water molecules, thus creating a passivating layer which protects metal iron inside the particles (Figure 7c).

We expect that this mechanism works with all immiscible elements having appreciable sticking coefficients between nuclei or for which the formation of mixed nuclei is possible during the fast ablation dynamics.

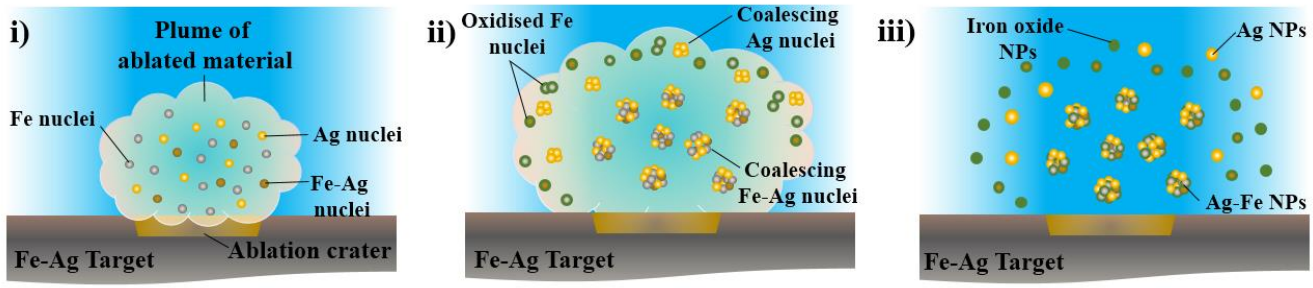

Figure 7. Sketch of the three stages of LASiS permitting the coexistence of the two immiscible elements in the same NPs: i) Formation of nuclei. After laser ablation of the target, hot nuclei containing Ag, Fe and mixed Ag and Fe are formed. In water, oxidation of iron occurs with high probability, whereas in ethanol this process is less probable due to the lower concentration of oxidising species. ii) Nuclei coalescence. Hot nuclei coalesce together and quickly cool down, forming solid NP with the structure of a partially melted aggregate. At the borders of the plasma plume, there is higher probability that iron is oxidised and a consequent lower probability of sticking with silver nuclei, thus avoiding the coexistence of iron and silver in the same nanostructures. iii) At longer times, surface oxidation of NP occurs by interaction with atmospheric oxygen or water molecules.

Conclusions.

We presented a synthetic strategy for the realization of multifunctional NPs composed by two immiscible elements of the periodic table: iron and silver. The synthesis occurs in one-step and exploits the fast kinetics of nanomaterials formation peculiar of LASiS. The Fe-Ag NPs have a truffle-like structure composed by a scaffold of fcc silver embedding metal iron and disordered silver-iron alloy domains. The surface of Fe-Ag nanotruffles is partly composed of iron oxide and partly of metal silver, thus allowing the functionalization in one pot with thiolated molecules. Overall, Fe-Ag NPs represent a multifunctional material endowed with magnetic and plasmonic properties, easy surface chemistry and a complete colloidal stability. Such a multifunctionality discloses a wide range of applications and, in particular, we exploited Fe-Ag NPs for the magnetic amplification of SERS signals. In aqueous solution, PEG-coated Fe-Ag NPs are efficient SERS substrates for cationic molecules and can be magnetically focused to further improve the Raman signal of one order of magnitude, enabling analyte detection down to $8 \cdot 10^{-8}$ M. The excellent colloidal stability of Fe-Ag NPs allowed also the regeneration and the sequential detection of different analytes with the same set of NPs. By tuning the surface coating of Fe-Ag NPs, we evidenced that PEG coating has a relevant role in the magnetic amplification, with better performances observed for incomplete Fe-Ag NPs surface coverage and shorter ligands.

Although the control of NPs size and phase is challenging, our synthetic approach is of general applicability, promising the preparation in one step of NPs containing all the desired elements. We

expect that, in the near future, this procedure will play an important role for the preparation of a wide range of new multifunctional nanostructures which are currently unavailable due to the unfavourable thermodynamics of mixing.

Experimental section.

Synthesis.

The laser ablation synthesis in solution (LASiS) was performed using 1064 nm (6 ns, 50 Hz) pulses of a Nd-YAG laser with a fluence of 6.7 J/cm^2. The pulses are focused with a 15 cm lens on a bimetallic target composed of 66at% of Ag and 34at% of Fe (from Mateck) placed at the bottom of a cell containing either distilled water or HPLC grade ethanol (>99.8% pure). The so obtained Fe-Ag NPs dispersion (0.1 mg/mL) was mixed with an aqueous solution containing disodium ethylenediaminetetraacetic acid (EDTA, from Sigma Aldrich, 2 mg/mL) and thiolated polyethyleneglycol (PEG, 0.01 mg/mL) and kept for 60 minutes at 30°C. We used thiolated PEG with molar mass of either 2000, 5000 and 20000 Da from Laysan Bio. Then, the Fe-Ag NPs dispersion was washed multiple times with distilled water by dialysis concentration membranes and finally resuspended in distilled water.

Fe-Ag NPs were magnetically sorted by placing a cylindrical NdFeB magnet (4 mm diameter for 8 mm length) below a 1 cm quartz cuvette containing the NPs dispersion. After 1 day of exposure, the supernatant (i.e. the non magnetic fraction) was separated from the material accumulated on the surface of the magnet (i.e. the magnetic fraction). The magnetic fraction was redispersed in distilled water.

For SERS experiments, the selective sedimentation protocol was applied to aqueous dispersion of Fe-Ag NPs following a previously established procedure.[63] For the selective sedimentation, we used 1.5 mL plastic centrifuge tubes, each filled with 1 mL of either magnetic or non magnetic Fe-Ag NPs solution, and an Eppendorf centrifuge model 5430 equipped with a fixed angle rotor model FA-45-24-11-HS. Solutions were centrifuged at 70 rcf for 1 hour, then the deposit was stored and redispersed in distilled water, while the supernatant was collected and centrifuged again at 126 rcf. The process was prosecuted in the same way at 250, 400 and 800 rcf.

Characterization.

UV-visible spectra were recorded with a Varian Cary 5 using quartz cells with a 2 mm optical path.

FTIR was performed with a Perkin Elmer 1720X, deposing the dried samples on a KBr window. Z-spectroscopy was performed with a Malvern Zetasizer Nano ZS. ICP-MS measurements were carried out with a Thermo Elemental X7 Series instrument equipped with the PlasmaLab software package. For instrument calibration, standard Fe and Ag solutions were purchased from Spectrascan.

Raman measurements for purposes of structural NPs characterization were recorded with a Renishaw inVia micro-Raman spectrometer on a dried powder of Fe-Ag NPs, using the 633 nm line of an He–Ne laser and 5X, 20X and 50X objectives. Laser power was increased from 1 mW to 13 mW in each analysis, in order to probe the initial iron phase (low power) and check for the formation of hematite (typically observed during high power laser irradiation of crystalline iron oxides),[64] although no peaks ascribable to iron oxides were detected in all cases.

TEM analysis was performed with a FEI Tecnai G2 12 operating at 100 kV and equipped with a TVIPS CCD camera. HRTEM, SAED and EDS analysis were carried out at 300 kV with a JEOL JEM 3010 microscope using a Gatan Multiscan CCD 794 Camera and an X-ray energy dispersive spectrometer (EDS, Oxford Instruments). The samples for TEM analysis were prepared by evaporating NPs suspensions on a copper grid coated with an amorphous carbon holey film.

EDS analysis and line scans were performed with a SEM model Zeiss Sigma VP equipped with a Bruker Quantax 200 detector (window size 30 mm^2) and a Silicon Drift Detector. The Ag L lines and the Fe K lines were considered for line scans and quantitative analysis.

XPS measurements were performed with a modified VG ESCALAB MKII (Vacuum generators, Hastings, England) equipped with a twin (Mg/Al) anode X-ray source, a sputter gun, and a hemispherical electrostatic analyzer with a five channel detector. We used the Al-Kα radiation (1486.6 eV) as an excitation source. Photoemission spectra have been obtained at room temperature using normal emission geometry. Prior to measurements, the samples were degassed overnight in the analysis chamber (pressure lower than 10^{-8} mbar). Samples were obtained by drying a droplet of Fe-Ag NPs dispersion at 40°C on a copper sample holder.

XRD patterns were collected with a Philips diffractometer constituted by an X'Pert vertical goniometer with Bragg–Brentano geometry, a focusing graphite monochromator and a proportional counter with a pulse-height discriminator. Nickel-filtered Cu Kα radiation and a step-by-step technique were used (steps of 2θ=0.05°), with collection times of 30 s per step. Line broadening analysis (LBA) was carried out using a previously published method,[65] whereas the Rietveld method for quantitative phase analysis exploited the DBWS9600 computer program written by Sakthivel and Young and modified by Riello et al.[66] The PDF file 000-06-0696 for Fe and 010-87-0597 for Ag were used.

Mossbauer spectroscopy was performed at room temperature using a conventional constant acceleration spectrometer with triangular waveform and a ^{57}Co source (nominal strength 1850 MBq) in a Rh matrix. The hyperfine parameters isomer shift (δ), quadrupole splitting (Δ) or quadrupole shift when magnetic splitting occurred (ε), half linewidth at half maximum ($\Gamma_{1/2}$), expressed in mms^{-1} and the internal magnetic field (B), expressed in Tesla, were obtained by means of standard least-squares minimization techniques. The spectra were fitted to Lorentzian line shapes with the minimum number of sextets and doublets. Isomer shift is quoted relative to α metallic iron at room-temperature.

Fluorescence XAS (X-ray Absorption Spectroscopy) data were collected at GILDA beamline (European Synchrotron Radiation Facility, ESRF, Grenoble, experimenti IHHC-2289) at the Fe-K edge (7112 eV).[67] A Si(311) double crystal monochromator was used; the harmonic rejection was realised by Pd mirrors, having a cut-off energy of 20 keV, and a 13-element Ge fluorescence detector. The energy calibration has been made by measuring the absorption spectrum of metallic Fe. For the measurements, the colloidal samples have been spotted onto Millipore filters and then cooled down to 100 K, aiming at increasing the EXAFS oscillations. The reproducibility in energy has been assured by measuring simultaneously the XAS spectra of a Fe foil, and for every scan found to be better than 0.1 eV. To obtain a reasonable signal to noise ratio, the integration time was adjusted to give ca. 10^6 counts in the fluorescence channel; in addition, in order to avoid distortions of the spectra, the count rate of each element was kept well below the saturation limit. The metal content were as low as ca. 100 $\mu g cm^{-2}$, and therefore self-absorption effects in the fluorescence spectra are in principle negligible. For the XANES analysis the spectra were processed by subtracting the smooth pre-edge background fitted with a straight line. The EXAFS extraction and data analysis were performed by means of the ATHENA[68] and EXCURVE[69] codes, respectively. The number of independent EXAFS points for the fit shown in this work is 11.

The magnetic properties were investigated on the samples in the form of dry powder using a Quantum Design MPMS XL-5 SQUID magnetometer. Zero-field-cooled (ZFC) magnetization curves were measured by cooling samples in zero magnetic field (H) and then by increasing the temperature in an applied field of 50 Oe, while field-cooled (FC) curves were recorded by cooling the samples in the same probe field. The field dependence of the magnetization (hysteresis loop) was recorded between ±50 kOe at T=300 K and 2.5 K. The saturation magnetization (M_s) was derived from a plot of M versus 1/H, extrapolating the M values for $1/H \rightarrow 0$.

Numerical calculations.

The Discrete Dipole Approximation (DDA) numerical calculations were performed with the DDSCAT 7.1 code,[70] using more than 10^5 dipoles for each target. The effect of water solvent has been accounted by setting the refractive index of the non-absorbing matrix n=1.334. The complex dielectric constant of Ag was taken from Palik.[71] We adopted a size-corrected dielectric constant to account for electron scattering at NPs surface, as reported in ref.[25]. The extinction spectra are computed considering unpolarized incident light.

SERS measurements.

SERS experiments were performed by mixing 0.5 mL of a 0.2 mg/mL Fe-Ag NPs dispersion with 0.1 mL of a 5 10^{-7} M solution of either 4-[(4-dimethylaminophenyl)phenyl-methyl]-*N*,*N*-dimethylaniline (MG, from Sigma Aldrich) or 1,1',3,3,3',3'-hexamethylindotricarbocyanine iodide (HITC, from Exciton). Raman measurements were collected at 633 nm, using a power of 3 mW, a 5X objective and a edge filter. At least three Raman measurements of 10 s each were collected on each sample placed in a 2 mm quartz cells. Fe-Ag NPs were magnetically focused by placing a cylindrical NdFeB magnet (2 mm diameter for 4 mm length) for 2 hours below a quartz cuvette containing the sample.

In case of the SERS spectra recorded cyclically on the same batch of Fe-Ag NPs, while alternating two different analytes (MG and HITC), the regeneration of the substrate took place each time with 3 centrifuge runs at 15000 rcf for 10 minutes with an aqueous solution of NaCl 10^{-4} M, to eliminate the analyte, followed by a cycle at 25000 rcf in distilled water for 10 minutes to eliminate the salt.

References

1. Lee, D.; Koo, H.; Sun, I.; Ryu, J. H.; Kim, K.; Kwon, I. C. Multifunctional nanoparticles for multimodal imaging and theragnosis. *Chem. Soc. Rev.* **2012**, *41*, 2656-2672.

2. Cheng, Z.; Al Zaki, A.; Hui, J. Z.; Muzykantov, V. R.; Tsourkas, A. Multifunctional nanoparticles: cost versus benefit of adding targeting and imaging capabilities. *Science* **2012**, *338*, 903-910.

3. Liu, K.; Jiang, L. Multifunctional integration: from biological to bio-inspired materials. *Acs Nano* **2011**, *5*, 6786-6790.

4. Armelles, G.; Cebollada, A.; Garcia-Martin, A.; Gonzalez, M. U. Magnetoplasmonics: Combining Magnetic and Plasmonic Functionalities. *Adv. Opt. Mater.* **2013**, *1*, 2-2.

5. Hao, R.; Xing, R.; Xu, Z.; Hou, Y.; Gao, S.; Sun, S. Synthesis, functionalization, and biomedical applications of multifunctional magnetic nanoparticles. *Adv. Mater.* **2010**, *22*, 2729-2742.

6. Peng, S.; Lei, C.; Ren, Y.; Cook, R. E.; Sun, Y. Plasmonic/magnetic bifunctional nanoparticles. *Angew. Chem. Int. Ed.* **2011**, *50*, 3158-3163.

7. García, S.; Zhang, L.; Piburn, G. W.; Henkelman, G.; Humphrey, S. M. Microwave Synthesis of Classically Immiscible Rhodium–Silver and Rhodium–Gold Alloy Nanoparticles: Highly Active Hydrogenation Catalysts. *ACS Nano* **2014**, *8*, 11512-11521.

8. González‐Díaz, J. B.; García‐Martín, A.; García‐Martín, J. M.; Cebollada, A.; Armelles, G.; Sepúlveda, B.; Alaverdyan, Y.; Käll, M. Plasmonic Au/Co/Au Nanosandwiches with Enhanced Magneto‐optical Activity. *Small* **2008**, *4*, 202-205.

9. Bonanni, V.; Bonetti, S.; Pakizeh, T.; Pirzadeh, Z.; Chen, J.; Nogués, J.; Vavassori, P.; Hillenbrand, R.; Åkerman, J.; Dmitriev, A. Designer magnetoplasmonics with nickel nanoferromagnets. *Nano letters* **2011**, *11*, 5333-5338.

10. Pineider, F.; Campo, G.; Bonanni, V.; de Julián Fernández, C.; Mattei, G.; Caneschi, A.; Gatteschi, D.; Sangregorio, C. Circular magnetoplasmonic modes in gold nanoparticles. *Nano letters* **2013**, *13*, 4785-4789.

11. Suntivich, J.; Xu, Z.; Carlton, C. E.; Kim, J.; Han, B.; Lee, S. W.; Bonnet, N.; Marzari, N.; Allard, L. F.; Gasteiger, H. A.; Hamad-Schifferli, K.; Shao-Horn, Y. Surface Composition Tuning of Au-Pt Bimetallic Nanoparticles for Enhanced Carbon Monoxide and Methanol Electro-oxidation. *J. Am. Chem. Soc.* **2013**, *135*, 7985-7991.

12. Amendola, V.; Scaramuzza, S.; Litti, L.; Meneghetti, M.; Zuccolotto, G.; Rosato, A.; Nicolato, E.; Marzola, P.; Fracasso, G.; Anselmi, C. Magneto‐Plasmonic Au‐Fe Alloy Nanoparticles Designed for Multimodal SERS‐MRI‐CT Imaging. *Small* **2014**.

13. Xu, C.; Wang, B.; Sun, S. Dumbbell-like Au−Fe3O4 nanoparticles for target-specific platin delivery. *J. Am. Chem. Soc.* **2009**, *131*, 4216-4217.

14. Sotiriou, G. A.; Visbal-Onufrak, M. A.; Teleki, A.; Juan, E. J.; Hirt, A. M.; Pratsinis, S. E.; Rinaldi, C. Thermal energy dissipation by SiO2-coated plasmonic-superparamagnetic nanoparticles in alternating magnetic fields. *Chem. Mater.* **2013**, *25*, 4603-4612.

15. Zhai, Y.; Han, L.; Wang, P.; Li, G.; Ren, W.; Liu, L.; Wang, E.; Dong, S. Superparamagnetic plasmonic nanohybrids: shape-controlled synthesis, TEM-induced structure evolution, and efficient sunlight-driven inactivation of bacteria. *ACS nano* **2011**, *5*, 8562-8570.

16. Bogani, L.; Cavigli, L.; de Julián Fernández, C.; Mazzoldi, P.; Mattei, G.; Gurioli, M.; Dressel, M.; Gatteschi, D. Photocoercivity of Nano‐Stabilized Au: Fe Superparamagnetic Nanoparticles. *Adv. Mater.* **2010**, *22*, 4054–4058.

17. Sarina, S.; Zhu, H.; Jaatinen, E.; Xiao, Q.; Liu, H.; Jia, J.; Chen, C.; Zhao, J. Enhancing Catalytic Performance of Palladium in Gold and Palladium Alloy Nanoparticles for Organic Synthesis Reactions through Visible Light Irradiation at Ambient Temperatures. *J. Am. Chem. Soc.* **2013**, *135*, 5793-5801.

18. Wang, C.; Yin, H.; Dai, S.; Sun, S. A General Approach to Noble Metal− Metal Oxide Dumbbell Nanoparticles and Their Catalytic Application for CO Oxidation. *Chem. Mater.* **2010**, *22*, 3277-3282.

19. Ferrando, R.; Jellinek, J.; Johnston, R. L. Nanoalloys: from theory to applications of alloy clusters and nanoparticles. *Chem. Rev.* **2008**, *108*, 845-910.

20. Carroll, K. J.; Hudgins, D. M.; Spurgeon, S.; Kemner, K. M.; Mishra, B.; Boyanov, M. I.; Brown III, L. W.; Taheri, M. L.; Carpenter, E. E. One-pot aqueous synthesis of Fe and Ag core/shell nanoparticles. *Chemistry of Materials* **2010**, *22*, 6291-6296.

21. Amendola, V.; Meneghetti, M. What controls the composition and the structure of nanomaterials generated by laser ablation in liquid solution? *Phys.Chem.Chem.Phys.* **2013**, *15*, 3027-3046.

22. Malviya, K. D.; Chattopadhyay, K. Synthesis and Mechanism of Composition and Size Dependent Morphology Selection in Nanoparticles of Ag-Cu Alloys Processed by Laser Ablation Under Liquid Medium. *J. Phys. Chem. C* **2014**, *118*, 13228-13237.

23. Amendola, V.; Meneghetti, M.; Bakr, O. M.; Riello, P.; Polizzi, S.; Fiameni, S.; Dalaver, H.; Arosio, P.; Orlando, T.; de Julian Fernandez, C.; Pineider, F.; Sangregorio, C.; Lascialfari, A. Coexistence of magnetic and plasmonic properties in Au89Fe11 nanoalloys. *Nanoscale* **2013**, *5*, 5611-5619.

24. Amendola, V.; Scaramuzza, S.; Agnoli, S.; Polizzi, S.; Meneghetti, M. Strong dependence of surface plasmon resonance and surface enhanced Raman scattering on the composition of Au-Fe nanoalloys. *Nanoscale* **2014**, *6*, 1423-1433.

25. Amendola, V.; Bakr, O. M.; Stellacci, F. A study of the surface plasmon resonance of silver nanoparticles by the discrete dipole approximation method: effect of shape, size, structure, and assembly. *Plasmonics* **2010**, *5*, 85-97.

26. Swartzendruber, L. The Ag− Fe (Silver-Iron) system. *J. Phas. Equil.* **1984**, *5*, 560-564.

27. Wan, H.; Tsoukatos, A.; Hadjipanayis, G.; Li, Z.; Liu, J. Direct evidence of phase separation in as-deposited Fe (Co)-Ag films with giant magnetoresistance. *Phys. Rev. B* **1994**, *49*, 1524.

28. Kataoka, N.; Sumiyama, K.; Nakamura, Y. Magnetic properties of high-concentration Fe-Ag alloys produced by vapour quenching. *J. Phys. F: Met. Phys.* **1985**, *15*, 1405.

29. Kataoka, N.; Sumiyama, K.; Nakamura, Y. Nonequilibrium crystalline Fe-Ag alloys vapour-quenched on liquid-nitrogen-cooled substrates. *J. Phys. F: Met. Phys.* **1988**, *18*, 1049.

30. Shi, Z.; Wang, T.; Lin, H.; Wang, X.; Ding, J.; Shao, M. Excellent surface-enhanced Raman scattering (SERS) based on AgFeO2 semiconductor nanoparticles. *Nanoscale* **2013**, *5*, 10029-10033.

31. Han, X. X.; Schmidt, A. M.; Marten, G.; Fischer, A.; Weidinger, I. M.; Hildebrandt, P. Magnetic Ag Hybrid Nanoparticles for Surface Enhanced Resonance Raman Spectroscopic Detection and Decontamination of Small Toxic Molecules. *ACS Nano* **2013**, *7*, 3212-3220.

32. Mahmoudi, M.; Serpooshan, V. Silver-coated engineered magnetic nanoparticles are promising for the success in the fight against antibacterial resistance threat. *ACS nano* **2012**, *6*, 2656-2664.

33. Murphy, C. J. Sustainability as an emerging design criterion in nanoparticle synthesis and applications. *J. Mater. Chem.* **2008**, *18*, 2173-2176.

34. Compagnini, G.; Scalisi, A. A.; Puglisi, O. Ablation of noble metals in liquids: a method to obtain nanoparticles in a thin polymeric film. *Phys.Chem.Chem.Phys.* **2002**, *4*, 2787-2791.

35. Amendola, V.; Riello, P.; Meneghetti, M. Magnetic Nanoparticles of Iron Carbide, Iron Oxide, Iron@ Iron Oxide, and Metal Iron Synthesized by Laser Ablation in Organic Solvents. *J Phys. Chem. C* **2011**, *115*, 5140–5146.

36. Amendola, V.; Polizzi, S.; Meneghetti, M. Free Silver Nanoparticles Synthesized by Laser Ablation in Organic Solvents and Their Easy Functionalization. *Langmuir* **2007**, *23*, 6766-6770.

37. Amendola, V.; Riello, P.; Polizzi, S.; Fiameni, S.; Innocenti, C.; Sangregorio, C.; Meneghetti, M. Magnetic iron oxide nanoparticles with tunable size and free surface obtained via a "green" approach based on laser irradiation in water. *J. Mater. Chem.* **2011**, *21*, 18665-18673.

38. Lim, J.; Majetich, S. A. Composite magnetic–plasmonic nanoparticles for biomedicine: Manipulation and imaging. *Nano Today* **2013**, *8*, 98-113.

39. Wiltner, A.; Linsmeier, C. Formation of endothermic carbides on iron and nickel. *Phys. Stat. Sol. (a)* **2004**, *201*, 881-887.

40. Maenosono, S.; Lee, J.; Dao, A. T. N.; Mott, D. Peak shape analysis of Ag 3d core‐level X‐ray photoelectron spectra of Au@ Ag core‐shell nanoparticles using an asymmetric Gaussian–Lorentzian mixed function. *Surf. Interface Anal.* **2012**, *44*, 1611-1614.

41. Grosvenor, A.; Kobe, B.; Biesinger, M.; McIntyre, N. Investigation of multiplet splitting of Fe 2p XPS spectra and bonding in iron compounds. *Surf. Interface Anal.* **2004**, *36*, 1564-1574.

42. Naitabdi, A.; Ono, L.; Behafarid, F.; Cuenya, B. R. Thermal Stability and Segregation Processes in Self-Assembled Size-Selected Au x Fe1-x Nanoparticles Deposited on TiO2 (110): Composition Effects. *J. Phys. Chem. C* **2009**, *113*, 1433-1446.

43. Santhi, K.; Thirumal, E.; Karthick, S.; Kim, H.; Narayanan, V.; Stephen, A. Structural and magnetic investigations on metastable Ag–Fe nanophase alloy. *J. Alloys Compounds* **2013**, *557*, 172-178.

44. Lebugle, A.; Axelsson, U.; Nyholm, R.; Mårtensson, N. Experimental L and M core level binding energies for the metals 22Ti to 30Zn. *Phys. Scripta* **1981**, *23*, 825.

45. Alonso, J.; Fdez-Gubieda, M.; Svalov, A.; Meneghini, C.; Orue, I. Effects of thermal annealing on the magnetic interactions in nanogranular Fe–Ag thin films. *J. Alloys Compounds* **2012**, *536*, S271-S276.

46. Wang, J.; Xiao, G. Transition-metal granular solids: Microstructure, magnetic properties, and giant magnetoresistance. *Phys. Rev. B* **1994**, *49*, 3982.

47. Spizzo, F.; Angeli, E.; Bisero, D.; Da Re, A.; Ronconi, F.; Vavassori, P. Mössbauer investigation of sputtered Fe< sub> x</sub> Ag< sub> 100− x</sub> films. *J Magn Magn Mater* **2004**, *272*, 1169-1170.

48. Tamisari, M.; Spizzo, F.; Sacerdoti, M.; Battaglin, G.; Ronconi, F. Correlation between structural and giant magnetoresistance properties of Fe–Ag nanogranular films. *J. Nanop. Res.* **2011**, *13*, 5203-5210.

49. Rixecker, G. The difficulty of isolating grain boundary components in the Mössbauer spectra of ball-milled materials: iron and silver–iron alloys. *Solid State Commun.* **2002**, *122*, 299-302.

50. Herr, U.; Jing, J.; Gonser, U.; Gleiter, H. Alloy effects in consolidated binary mixtures of nanometer-sized crystals investigated by Mössbauer spectroscopy. *Solid State Commun.* **1990**, *76*, 197-202.

51. Binns, C.; Maher, M.; Pankhurst, Q.; Kechrakos, D.; Trohidou, K. Magnetic behavior of nanostructured films assembled from preformed Fe clusters embedded in Ag. *Phys. Rev. B* **2002**, *66*, 184413.

52. Amendola, V.; Meneghetti, M. Exploring How to Increase the Brightness of Surface-Enhanced Raman Spectroscopy Nanolabels: the Effect of the Raman-Active Molecules and of the Label Size. *Adv. Funct. Mater.* **2012**, *22*, 353-360.

53. Stamplecoskie, K. G.; Scaiano, J. C.; Tiwari, V. S.; Anis, H. Optimal size of silver nanoparticles for surface-enhanced Raman spectroscopy. *J. Phys. Chem. C* **2011**, *115*, 1403-1409.

54. Yudanov, I. V.; Metzner, M.; Genest, A.; Rösch, N. Size-dependence of adsorption properties of metal nanoparticles: a density functional study on palladium nanoclusters. *J. Phys. Chem. C* **2008**, *112*, 20269-20275.

55. Panizon, E.; Bochicchio, D.; Rossi, G.; Ferrando, R. Tuning the structure of nanoparticles by small concentrations of impurities. *Chem. Mater.* **2014**.

56. Wagener, P.; Ibrahimkutty, S.; Menzel, A.; Plech, A.; Barcikowski, S. Dynamics of silver nanoparticle formation and agglomeration inside the cavitation bubble after pulsed laser ablation in liquid. *Phys.Chem.Chem.Phys.* **2013**, *15*, 3068-3074.

57. Compagnini, G.; Messina, E.; Puglisi, O.; Nicolosi, V. Laser synthesis of Au/Ag colloidal nano-alloys: Optical properties, structure and composition. *Appl. Surf. Sci.* **2007**, *254*, 1007-1011.

58. Tiedemann, D.; Taylor, U.; Rehbock, C.; Jakobi, J.; Klein, S.; Kues, W. A.; Barcikowski, S.; Rath, D. Reprotoxicity of gold, silver, and gold–silver alloy nanoparticles on mammalian gametes. *Analyst* **2014**, *139*, 931-942.

59. Capelo, R. G.; Leppert, L.; Albuquerque, R. Q. d. On the Concept of Localized Atomic Mobility: Unraveling Properties of Nanoparticles. *J. Phys. Chem. C* **2014**, *118*, 21647-21654.

60. Link, S.; Burda, C.; Nikoobakht, B.; El-Sayed, M. A. Laser-Induced Shape Changes of Colloidal Gold Nanorods Using Femtosecond and Nanosecond Laser Pulses. *J Phys Chem B* **2000**, *104*, 6152-6163.

61. Andrews, M. P.; O'Brien, S. C. Gas-phase" molecular alloys" of bulk immiscible elements: iron-silver (FexAgy). *J. Phys. Chem.* **1992**, *96*, 8233-8241.

62. Amendola, V.; Meneghetti, M.; Granozzi, G.; Agnoli, S.; Polizzi, S.; Riello, P.; Boscaini, A.; Anselmi, C.; Fracasso, G.; Colombatti, M. Top-down synthesis of multifunctional iron oxide nanoparticles for macrophage labelling and manipulation. *J. Mater. Chem.* **2011**, *21*, 3803-3813.

63. Bonaccorso, F.; Zerbetto, M.; Ferrari, A. C.; Amendola, V. Sorting nanoparticles by centrifugal fields in clean media. *J. Phys. Chem. C* **2013**, *117*, 13217-13229.

64. McCarty, K. F.; Monti, M.; Nie, S.; Siegel, D. A.; Starodub, E.; El Gabaly, F.; McDaniel, A. H.; Shavorskiy, A.; Tyliszczak, T.; Bluhm, H. Oxidation of Magnetite (100) to Hematite Observed by In-situ Spectroscopy and Microscopy. *J. Phys. Chem. C* **2014**, *118*, 19768-19777.

65. Enzo, S.; Polizzi, S.; Benedetti, A. Applications of fitting techniques to the Warren-Averbach method for X-ray line broadening analysis. *Z. Kristallogr.* **1985**, *170*, 275-287.

66. Riello, P.; Canton, P.; Fagherazzi, G. Quantitative Phase Analysis in Semicrystalline Materials Using the Rietveld Method. *J. Appl. Crystallogr.* **1998**, *31*, 78-82.

67. D'Acapito, F.; Colonna, S.; Pascarelli, S.; Antonioli, G.; Balerna, A.; Bazzini, A.; Boscherini, F.; Campolungo, F.; Chini, G.; Dalba, G.; Davoli, I.; Fornasini, P.; Graziola, R.; Licheri, G.; Meneghini, C.; Rocca, F.; Sangiorgio, L.; Sciarra, V.; Tullio, V.; Mobilio, S. *ESRF Newsletter* **1998**, *30*, 42-44.

68. Anonymous*http://cars9.uchicago.edu/~ravel/software/exafs/* .

69. Binsted, N.; Gurman, S. J.; Campbell, T. C.; Stephenson, P. C. *EXCURV98 program (Daresbury: SERC Daresbury Laboratory)* **1998**.

70. Draine, B.; Flatau, P. User Guide to the Discrete Dipole Approximation Code DDSCAT 7.1, 2010./h ttp. *arxiv.org/abs/1002.1505v1 S* .

71. Palik, E. D. *Handbook of Optical Constants of Solids;* Academic Press: 1985; .